

# One-neutron transfer study of $^{137}\text{Xe}$ and systematics of $13/2_1^+$ and $13/2_2^+$ levels in $N = 83$ nuclei

W. Reviol<sup>1</sup>, D. G. Sarantites<sup>1</sup>, J. M. Elson<sup>1</sup>, J. E. Kinnison<sup>1</sup>, A. Gargano<sup>2</sup>, S. Bottoni<sup>3,4</sup>,  
R. V. F. Janssens<sup>3</sup>, J. M. Allmond<sup>5</sup>, D. Ayangeakaa<sup>3</sup>, M. P. Carpenter<sup>3</sup>, H. M. David<sup>3,\*</sup>,  
A. Galindo-Uribarri<sup>5</sup>, N. Itaco<sup>2,6</sup>, T. Lauritsen<sup>3</sup>, E. Padilla-Rodal<sup>7</sup>, and S. Zhu<sup>3</sup>

<sup>1</sup>*Department of Chemistry, Washington University, St. Louis, MO 63130, USA*

<sup>2</sup>*Instituto Nazionale di Fisica Nucleare,*

*Complesso Universitario di Monte S. Angelo, Via Cintia, I-80126 Napoli, Italy*

<sup>3</sup>*Physics Division, Argonne National Laboratory, Argonne, IL 60439, USA*

<sup>4</sup>*Universita degli Studi di Milano, Via Celoria 16, Milano 20133, Italy*

<sup>5</sup>*Physics Division, Oak Ridge National Laboratory, Oak Ridge, TN 37831, USA*

<sup>6</sup>*Dipartimento di Matematica e Fisica,*

*Seconda Universita di Napoli, Caserta, Italy*

<sup>7</sup>*Instituto de Ciencias Nucleares, UNAM, 04510 Mexico, D.F., Mexico*

(Dated: April 27, 2016)

## Abstract

Excited states in  $^{137}\text{Xe}$  have been studied by using the near-barrier, single-neutron transfer reactions  $^{13}\text{C}(^{136}\text{Xe},^{12}\text{C}\gamma)^{137}\text{Xe}$  and  $^9\text{Be}(^{136}\text{Xe},^8\text{Be}\gamma)^{137}\text{Xe}$  in inverse kinematics. Particle- $\gamma$  and particle- $\gamma\gamma$  coincidence measurements have been performed with the Phoswich Wall and Digital Gammasphere detector arrays. Evidence is found for a  $13/2_2^+$  level ( $E = 3137$  keV) and for additional, high-lying  $3/2^-$  and  $5/2^-$  states. The results are discussed in the framework of realistic shell-model calculations. These calculations are also extended to the  $13/2_1^+$  and  $13/2_2^+$  levels in the  $N = 83$  isotonic chain. They indicate that there is a need for a value of the neutron  $0i_{13/2}$  single-particle energy ( $E_{SPE} = 2366$  keV) lower than the one proposed in the literature. It is also demonstrated that the population patterns of the  $j = \ell \pm 1/2$  single-particle states in  $^{137}\text{Xe}$  are different for the two targets used in these measurements and the implications of this effect are addressed.

PACS numbers: 27.80.+w, 27.90.+b, 23.20.Lv, 21.60.Ev

---

\*Present address: Gesellschaft fuer Schwerionenforschung, Darmstadt, Germany

## I. INTRODUCTION

New developments in instrumentation and experimental techniques for precision spectroscopy have recently enabled progress in the identification of single-neutron states in the  $^{132}\text{Sn}$  ( $Z = 50, N = 82$ ) region – see e.g., Refs. [1–5]. As a result, for the  $N = 83$  odd-mass nuclei from Sn to Sm ( $Z = 62$ ), a nearly complete set of energy levels and spectroscopic factors related to the orbitals of interest is now available; i.e., for the  $1f_{7/2}, 2p_{3/2}, 2p_{1/2}, 1f_{5/2}, 0h_{9/2}$ , and the unique-parity  $0i_{13/2}$  states. In a few cases, such as  $^{133}\text{Sn}$ , excited-state lifetime information has been obtained as well [5]. This body of data has provided stringent tests of shell-model calculations [6, 7], herewith improving their predictive power for properties of even more neutron-rich nuclei in this region.

While the systematics of the single-particle states in the  $N = 82 - 126$  shell appears to be by now fairly complete, issues remain with the  $0i_{13/2}$  orbital and the corresponding single-particle energy. Strictly speaking, this quantity should be derived from the energy spectrum of a nucleus with a single valence particle. However, the  $13/2^+$  state in  $^{133}\text{Sn}$  has not yet been observed. Due to this lack of information, researchers have resorted to (and reached meaningful conclusions from) the three available “sources” that shed light on the neutron  $0i_{13/2}$  single-particle energy: (i) the  $10^+$  level in  $^{134}\text{Sb}$  with a presumably dominant proton-neutron configuration  $(\pi g_{7/2} \nu i_{13/2})_{10^+}$  [8, 9]; (ii) the  $27/2^-$  and  $29/2^-$  states in  $^{135}\text{Sb}$  likely associated with the configurations  $(\pi g_{7/2} \nu [i_{13/2} f_{7/2}]_{10^-})_{27/2^-}$  and  $(\pi g_{7/2} \nu [i_{13/2} h_{9/2}]_{11^-})_{29/2^-}$ , respectively [10]; and (iii) the first  $13/2^+$  level in  $^{135}\text{Te}$  and heavier odd-mass  $N = 83$  nuclei [4]. These types of information are complementary to each other, and all of them should be considered when dealing with the  $\nu 0i_{13/2}$  orbital.

The subject of the present study is  $^{137}\text{Xe}$  ( $Z = 54$ ). For the description of the  $13/2_1^+$  level in the  $N = 83$  isotones, the interaction and mixing with a higher-lying, second  $13/2^+$  state should be taken into account [11]. This  $13/2_2^+$  state is expected to be primarily composed of members of the  $2^+ \otimes 0i_{13/2}$  and  $3^- \otimes 1f_{7/2}$  multiplets [11]. These configurations represent quadrupole and octupole vibrational excitations of the  $N = 82$  “core” coupled, correspondingly, to the  $13/2^+$  excited and  $7/2^-$  ground state of the  $N = 83$  system. For example, in  $^{137}\text{Xe}$  the expected  $13/2_1^+ - 13/2_2^+$  admixture and the uncertainty of the single-particle energy of the neutron used in calculations are thought to be responsible for the comparatively poor agreement between the measured and predicted  $13/2_1^+$  level energy [6]. Note that the

same work [6] indicates good agreement between theory and experiment for all the other states of interest. To address these issues, the location of the  $13/2_2^+$  level in  $^{137}\text{Xe}$  is helpful.

Previous experimental studies of  $^{137}\text{Xe}$  have been carried out with an emphasis on the high-spin yrast sequence [12], on the low-spin structure [3, 13], and on the precise location of the  $13/2_1^+$  intruder state [4]; the resulting level scheme is proposed in Ref. [14]. The present study follows the experimental approach of Ref. [4]; i.e., it uses one-neutron transfer reactions in inverse kinematics with a  $^{136}\text{Xe}$  beam on two different targets,  $^{13}\text{C}$  and  $^9\text{Be}$ . The observed difference in the population of excited states in  $^{137}\text{Xe}$  is analyzed in detail, while new levels are reported, including the  $13/2_2^+$  level of interest. The experimental findings are complemented by shell-model calculations. A lower value of the  $\nu 0i_{13/2}$  single-particle energy than that used in Ref. [8] is introduced to calculate both the  $13/2_1^+$  and  $13/2_2^+$  states for a series of odd-mass  $N = 83$  nuclei, and the energy levels in  $^{134,135}\text{Sb}$  associated with the  $i_{13/2}$  orbital. The overall agreement between theory and experiment is found to be satisfactory. The comparison of the results obtained with the two  $0i_{13/2}$  energy values used in the calculations allows one to propose a realistic range for the  $\nu 0i_{13/2}$  single-particle energy.

The  $13/2_2^+$  level is observed only with the  $^{13}\text{C}$  target. Likewise, the data indicate that the population of the  $13/2_1^+$  state is enhanced when compared to the data set from the  $^9\text{Be}$  target. The present study was carried out, in part, with the intent to verify that the different population patterns follow the  $\ell$ - and  $j$ -selection rules for nucleon transfer discussed in Ref. [15]. For example, the population of a  $0i_{13/2}$ ,  $j = \ell + 1/2$  ( $j_>$ ) state is expected to be more likely with the odd nucleon (of either the target or the beam) residing in a  $j = \ell - 1/2$  ( $j_<$ ) rather than a  $j_>$  orbital. Hence, by using a  $^{13}\text{C}$  target with a  $0p_{1/2}$  ( $j_<$ ) valence neutron, a transfer to the  $0i_{13/2}$  orbital is favored over that to the available  $j_<$  orbitals. Conversely, using the same beam and a  $^9\text{Be}$  target, with a  $0p_{3/2}$  ( $j_>$ ) valence neutron, should introduce a preference for feeding the  $j_<$  orbitals, such as the  $2p_{1/2}$  and  $1f_{5/2}$  ones, in  $^{137}\text{Xe}$ .

## II. EXPERIMENTAL CONDITIONS AND ANALYSIS PROCEDURES

The experiment was performed at the ATLAS accelerator at Argonne National Laboratory. A 560-MeV  $^{136}\text{Xe}$  beam impinged on two targets: a  $^{13}\text{C}$  foil with 99 % isotopic enrichment and 0.15-mg/cm<sup>2</sup> thickness and a mono-isotopic, 1.5-mg/cm<sup>2</sup>  $^9\text{Be}$  foil. The

beam intensities were 500 and 70 ppA and the runs took 40 and 14 h with the  $^{13}\text{C}$  and  $^9\text{Be}$  targets, respectively. The detection setup comprised Digital Gammasphere [16], with 92 Compton-shielded HPGe detectors arranged in 16 angular rings around the target [17], and the Phoswich Wall, a 256-element, fast-plastic + CsI(Tl) charged-particle detector array [18]. The latter array was located downstream from the target, with a lab-angle coverage of  $9^\circ \leq \theta_{lab} \leq 72^\circ$ , and enabled the correlation of a specific target-like fragment (TLF) with coincident  $\gamma$  rays emitted by the corresponding projectile-like fragment (PLF). The event trigger required that a Phoswich Wall element and at least two HPGe detectors fired prior to suppressing Compton-scattering signals.

In the offline analysis, a gating procedure was applied to the so-called (A,C) particle map, a combination of the fast-plastic and “late” CsI(Tl) signals (see Ref. [18] for details), *and* the prompt peak of the time spectrum of the measured particle with respect to the accelerator radiofrequency. The map gating condition for the different runs required the presence of TLF carbon or  $^8\text{Be} \rightarrow 2\alpha$  events. The Doppler-shift correction applied to the  $\gamma$ -ray spectra relied on the PLF velocity vector reconstructed event-by-event for the binary reaction, and took advantage of the high degree of pixelation of the Phoswich Wall.

For each run, two types of two-dimensional histograms of  $\gamma$ -ray energies were created: (i) an  $E_\gamma - E_\gamma$  matrix and (ii) a set of “angle-dependent”  $E_\gamma(\chi) - E_\gamma(\text{any})$  matrices. The matrices in (ii) allowed to measure the  $\gamma$ -ray anisotropies relative to the spin direction of the fragment nucleus following the procedure of Ref. [19]. Here,  $\chi$  represents the angle between the emitted  $\gamma$  ray and the spin direction (binned into  $10^\circ$  increments), while “any” stands for no angle requirement. All these histograms were analyzed using the RADWARE analysis package [20].

### III. EXPERIMENTAL RESULTS

This section reports the new information on the  $^{137}\text{Xe}$  level scheme obtained in the present experiment. As different population patterns were observed for the excited states in  $^{137}\text{Xe}$  as a function of the target used, the information is summarized in two separate diagrams.

Representative  $\gamma$ -ray spectra for the desired one-neutron transfer channel in both reactions are provided in Figs. 1 and 2, respectively, and are used to justify the locations of new transitions in the level schemes of Fig. 3. The total projection in panel (a) of Fig. 1

has been produced with a carbon gate and the strongest  $\gamma$  rays correspond to one-neutron pick-up and transfer ( $^{135,137}\text{Xe}$ ) as well as to projectile Coulomb excitation ( $^{136}\text{Xe}$ ). In the case of  $^{135}\text{Xe}$ , some of the  $\gamma$  rays are only assigned tentatively and labeled as such by a filled symbol. In addition to the xenon nuclei, the proton-transfer product  $^{137}\text{Cs}$  and, in a lesser amount, the  $^{139,140}\text{Ba}$  nuclei are present as well; the latter originate from  $^{136}\text{Xe} + \alpha$  or  $^5\text{He}$  incomplete fusion reactions. In these cases,  $^{12}\text{B}$  ( $^{137}\text{Cs}$ ) or one of the remaining  $^9\text{Be}$  or  $^8\text{Be}$  fragments ( $^{139,140}\text{Ba}$ ) was detected and has leaked into the particle coincidence gate.

Panels (b) and (c) display carbon- and  $\gamma$ -gated spectra for  $^{137}\text{Xe}$ . The spectrum gated on the 1220-keV ground-state transition (panel [b]) displays the expected lines [4, 14] and, in addition, a new 1384-keV  $\gamma$  ray. In turn, the 1384-keV gate of panel c shows the 533- and 1220-keV lines only. This observation requires the placement of the new  $\gamma$  ray on top of the 533-keV,  $13/2^+ \rightarrow 11/2^-$  transition, as proposed in panel (a) of Fig. 3.

Figure 2 presents a set of representative  $^{137}\text{Xe}$  spectra from the  $^9\text{Be}$  data. The total projection of panel (a) is dominated by the 601- and 385-keV transitions from the first and second excited states in  $^{137}\text{Xe}$ . These states are crucial for determining the low-spin part of the level scheme. A comparison of the intensities of the 601- and 1220-keV ground-state transitions with those in panel (a) of Fig. 1 confirms that the choice of the two targets leads to the anticipated differences in the population pattern of the nucleus (see Table I and related discussion). In Fig. 2 (a), binary-reaction products other than  $^{137}\text{Xe}$  are also substantially reduced. Note that projectile Coulomb excitation is excluded by the coincidence requirement of  $2\alpha$  events. Hence, the competing reaction channels are mainly those resulting from incomplete fusion. In this context, the Ce lines are attributed to  $^{136}\text{Xe}$  reactions on the oxygen originating from target oxidation.

Panels (b) and (c) display  $2\alpha$ - and  $\gamma$ -gated coincidence spectra for  $^{137}\text{Xe}$ . The coincidence spectrum gated by the 385-keV line leads to the observation of new  $^{137}\text{Xe}$  transitions with respective energies  $E_\gamma = 863, 1324, 1579, \text{ and } 1963$  keV. In addition, the spectrum gated by the 601-keV ground-state transition (not shown) suggests that a weak 2349-keV  $\gamma$  ray bypasses the 1963-keV transition. A spectrum gated on one of these new transitions ( $E_\gamma = 1579$  keV) is presented in panel (c): it shows the 385- and 601-keV lines only. The 1579-keV transition confirms the existence of a previously reported level ( $E = 2567$  keV). Likewise, the 863-keV  $\gamma$  ray represents a newly observed decay branch of a known state, while the 1324-keV line, and the 1963- and 2349-keV pair of transitions establish two new levels.

For most of the newly observed transitions, spin and parity assignments are proposed based on a  $\gamma$ -ray angular-distribution analysis. Figure 4 provides sample angular distributions for three  $\gamma$  rays measured in the carbon data: a known stretched dipole (a) and quadrupole (b) transition, and the newly observed 1384-keV line (c). These have been fitted with a standard Legendre polynomial expression and the fit results are included in the figure. The characteristic  $A_2/A_0$  and  $A_4/A_0$  coefficients derived from the fits are reported in Table I, together with other information on the transitions of interest. Values obtained for known transitions (Fig. 4 [a] and [b]) are in line with expectations. The angular distribution of the 1384-keV transition is consistent with either a quadrupole ( $E2$ ) or an unstretched-dipole (no spin change) assignment. The latter is preferred, based on the large value of the  $A_4/A_0$  coefficient, and a  $13/2_2^+$  assignment follows for the 3137-keV level. Interestingly, the  $13/2_2^+$  states in the  $N = 83$  isotones  $^{143}\text{Nd}$  and  $^{145}\text{Sm}$  also decay to the respective  $13/2_1^+$  levels [14], providing further support for the assignment.

In the present study, the assignments of important known transitions have been confirmed as well. For the 986-keV level, the  $A_2/A_0$  coefficient of the 385-keV line is consistent with 0 indicating an isotropic transition from this state and supporting a  $1/2^-$  assignment. This removes the previous  $1/2^-, 3/2^-$  ambiguity [3]. (The isotropy of the 601-keV,  $3/2^- \rightarrow 7/2^-$  transition is attributed to the loss of alignment due the recoil-in-vacuum effect for this  $\gamma$  ray at the bottom of the cascade.) The 1936-keV level is reassigned as  $5/2^-$  since the rather strong 951-keV  $\gamma$  ray is of quadrupole ( $E2$ ) character.

The decay of the 1879-keV level to the  $11/2_1^-$ , 1220-keV state is confirmed; the 659-keV transition has an intensity  $I_\gamma = 4.5(6)$  in the  $^{13}\text{C}$  measurement ( $I_\gamma \lesssim 3$  in the  $^9\text{Be}$  run). This 1879-keV state is tentatively assigned  $11/2$  based on intensity considerations. An alternative  $13/2$  assignment seems to be ruled out since, in the  $^{13}\text{C}$  measurement, this 1879-keV level is less populated than the  $13/2_2^+$  off-yrast state. Similarly, a  $9/2$  assignment appears unlikely in view of (i) the weak population of the  $9/2_1^-$ , 1218-keV level, which is comparable to the intensity of the 659-keV transition (see below), and (ii) the non-observation of the ( $9/2_2^-$ ), 1590-keV level in the present experiment. Hence, the 1879-keV level is viewed as a candidate for the  $11/2_2^-$  state.

The lowest-lying states of single-particle character in  $^{137}\text{Xe}$  are populated with both targets, but with markedly different strengths: in the  $^{13}\text{C}$  measurement, the  $13/2_1^+$  level ( $0i_{13/2}$  candidate) and the  $11/2_1^-$  state to which it decays are prominently present whereas,

in the  ${}^9\text{Be}$  data, these states are weakly populated compared to the  $5/2_1^-$  ( $1f_{5/2}$ ),  $1/2^-$  ( $2p_{1/2}$ ), and  $3/2_1^-$  ( $2p_{3/2}$ ) levels. Despite this difference in the population patterns of the single-particle states, the  ${}^{13}\text{C}$  and  ${}^9\text{Be}$  measurements share the common feature that the known high-spin yrast levels, which feed the  $11/2_1^-$  state [12], are suppressed. Specifically, the populations of the  $15/2^-$ , 1620-keV level and its feeder states is not competitive with that of the  $13/2_1^+$  level. The present findings are depicted in Fig. 5, where the decay intensity for a given level is plotted as a function of the excitation energy. Here, corrections for internal conversion have been applied, where possible. These are small compared to the uncertainties of the  $\gamma$ -ray intensities.

Note that the  $3/2^-$ ,  $5/2^-$ , 1716-keV (decay-intensity  $\leq 6$ ) and  $(11/2)$ , 1879-keV levels, have been excluded from Fig. 5 for simplicity. Both the  ${}^{13}\text{C}$  and  ${}^9\text{Be}$  measurements also provide evidence for the population of the  $9/2_1^-$ , 1218-keV level, which is partially fed by transitions with  $E_\gamma = 578, 773, 812,$  and  $870$  keV (cf. Fig. 1 [b]) and directly decays to the ground state [14]. However, as was the case in Ref. [3], the population of the  $9/2_1^-$  level ( $0h_{9/2}$  candidate) is weak with respect to, e.g., the  $5/2_1^-$  level as the aforementioned feeder transitions have a combined intensity  $\Sigma I_\gamma \lesssim 3$ . In view of these low intensities, it is not possible to draw a conclusion about a potential difference in the population of the  $9/2_1^-$  level between the two data sets.

## IV. DISCUSSION

### A. Differences in the two reactions

The differing population patterns of Fig. 5 follow the  $\ell$ - and  $j$ -selection rules expected for one-nucleon transfer [15]. Clearly, the  $0i_{13/2}$  ( $j_>$ ) state is populated more strongly with the  ${}^{13}\text{C}$  target, where the valence neutron occupies the  $0p_{1/2}$  ( $j_<$ ) orbital, whereas, for the  ${}^9\text{Be}$  target with its odd  $0p_{3/2}$  ( $j_>$ ) neutron, the states in  ${}^{137}\text{Xe}$  based on the  $2p_{1/2}$  and  $1f_{5/2}$  ( $j_<$ ) orbitals are preferred. In the following considerations, the net intensity, obtained from the total intensities out of and into a level ( $I_{net} = \Sigma I_{out} - \Sigma I_{in}$ ), is taken as a measure of the direct population of the state of interest. This quantity is, after a common normalization, compared with the cross sections from distorted wave Born approximation (DWBA) calculations. The latter were performed with the FRESKO code [21], where the

mid-target energies of the reactions were used and the assumption was made that the states are based on pure single-neutron configurations. The pertinent details of this comparison are summarized in Table II. The  $I_{net}$  values commonly represent a considerable fraction ( $\sim 1/2$  to  $3/4$ ) of the corresponding decay intensities in Fig. 5. Hence, each part of the present comparison is affected by unobserved side feeding, but to a comparable degree. Uncertainties in the calculations on the spectroscopic factors impact the comparison as well. (The  $I_{net}$  values for the  $3/2^-$  state, which are not part of the present comparison, are close to zero.) Given that the procedure has limited accuracy, the  $I_{net}^{rel}$  and  $\sigma_{DWBA}^{rel}$  values of Table II exhibit a reasonably close correspondence. Particularly, the very different relative yields for the  $13/2_1^+$  level in the two reactions are accounted for.

The weak population of the yrast states with  $I \geq 15/2$  can, perhaps, be explained in a similar fashion. Since the ground states of  $^{137}\text{Xe}$  and the target correspond to orbital angular momenta  $\ell = 3$  and 1, respectively, the angular-momentum transfer should not exceed a total value of 4; i.e., a spin difference of  $15/2 - 7/2$ .

## B. Comparisons with shell model calculations

In this section, a comparison is carried out between, on the one hand, the experimental  $13/2_1^+$  and  $13/2_2^+$  levels in  $^{137}\text{Xe}$  and the neighboring isotones and, on the other hand, the results of realistic shell-model calculations. The new information on other levels in  $^{137}\text{Xe}$  is addressed by the calculations as well.

The relevant  $N = 83$  systematics are presented in Fig. 6. Besides  $^{137}\text{Xe}$ , the  $13/2_2^+$  states have been established in the neighboring odd-mass nuclei  $^{143}\text{Nd}$  and  $^{145}\text{Sm}$  ( $Z = 60, 62$ ), while candidate  $13/2_2^+$  levels are reported for  $^{139}\text{Ba}$ ,  $^{141}\text{Ce}$ , and  $^{147}\text{Gd}$  ( $Z = 56, 58, \text{ and } 64$ ) [14]. For the latter levels, the decay is unknown and/or the spin-parity assignment is uncertain. In Fig. 6, these  $13/2_1^+$  and  $13/2_2^+$  levels are also compared with the results of realistic shell-model calculations. The latter use the two-body effective Hamiltonian introduced in Ref. [6]. These matrix elements were derived with the help of the CD-Bonn nucleon-nucleon potential [22] within a model space including the  $0g_{7/2}, 1d, 2s, 0h_{11/2}$  and  $1f, 2p, 0h_{9/2}, 0i_{13/2}$  orbitals for protons and neutrons, respectively. As in Ref. [6], the adopted single-proton and single-neutron energies were taken, where possible, from inspection of the  $^{133}\text{Sb}$  and  $^{133}\text{Sn}$  level schemes [14]. However, the  $\pi s_{1/2}$  and  $\nu i_{13/2}$  energies are not available

yet from these two semi-magic nuclei and, thus, additional information is needed. The position of the proton  $2s_{1/2}$  orbital was determined based on the  $1/2^+$ , 2150-keV level in  $^{137}\text{Cs}$  [23]. For the position of the neutron  $0i_{13/2}$  orbital, two alternative procedures have been used here and the corresponding calculations are referred to hereafter as “calc1” and “calc2”. For the “calc1” computations, the  $\nu 0i_{13/2}$  energy was estimated based on the  $10^+$  level in  $^{134}\text{Sb}$ , which has been assigned a  $\pi g_{7/2}\nu i_{13/2}$  configuration and is located at 2434 keV with respect to the yrast  $7^-$  state [8, 9]. This procedure leads to a value of 2694 keV and is the same as that adopted in Ref. [6]. For the “calc2” calculations, the estimate has been modified such that the energy of the  $13/2_1^+$  level in  $^{137}\text{Xe}$  is reproduced. In this context, this  $13/2_1^+$  level is essentially described as a  $0i_{13/2}$  neutron coupled to the proton wavefunction, which represents the core; i.e., its amplitude is 92% in the total wavefunction, as discussed further below. The adopted value of the  $\nu 0i_{13/2}$  single-particle energy (SPE) is 2366 keV in this approach.

Focussing first on the  $13/2_1^+$  state, the calculations with the two effective interactions display (Fig. 6) the same general trend with proton number, with the “calc2” results being in general closer to the data than the “calc1” ones because of the choice of the  $\nu 0i_{13/2}$  single-particle energy. The agreement between experiment and theory, while satisfactory for  $^{135}\text{Te}$  and  $^{137}\text{Xe}$ , becomes gradually poorer for  $Z > 56$ . This is likely, in part, due to the fact that the two-body effective interaction has been derived from data on systems with two valence nucleons, which may be less adequate for the description of nuclei with a larger number of such nucleons where many-body effects could play a role. In addition, as  $Z$  increases, the nature of the  $13/2_1^+$  state itself may well be changing, as discussed further below. Regarding the  $13/2_2^+$  level, a dependence on the  $\nu 0i_{13/2}$  single-particle energy is visible only at low  $Z$ , e.g., for  $^{135}\text{Te}$  and  $^{137}\text{Xe}$ , with the “calc2” results closer to the data than the “calc1” ones. Thus, the trend exhibited by the experimental data for the  $13/2_2^+$  levels as a function of  $Z$  is reproduced well in general, with the largest discrepancies occurring closer to  $Z = 50$ , a behavior opposite to that noted for the  $13/2_1^+$  states.

The applicability of the “calc2” approach was checked further for the relevant states in  $^{134}\text{Sb}$  and  $^{135}\text{Sb}$ , and the results are summarized in Table III. For the  $10^+$  state in  $^{134}\text{Sb}$ , the “calc1” energy is closer to the adopted experimental value of 2713 keV than the value computed for “calc2”. On the other hand, a better agreement is reached for the  $27/2^-$  and  $29/2^-$  experimental levels in  $^{135}\text{Sb}$  with the “calc2” calculations. This finding

presumably illustrates the fact that an optimal value for the  $\nu 0i_{13/2}$  single-particle energy has yet to be found. However, it also suggests that a value lower than the one proposed in the literature,  $E_{SPE} = 2694$  keV [6], is required. From the discussion above, it can be concluded that the recommended value for the  $\nu 0i_{13/2}$  single-particle energy to be used in shell-model calculations for  $N = 83$  and  $84$  nuclei should be in the  $2360 \text{ keV} \leq E_{SPE}(\nu 0i_{13/2}) \leq 2600$  keV range.

As alluded to above, the character of the  $13/2_1^+$  state may well be changing as  $Z$  increases. Figure 7 presents the “calc2” values of the  $\nu 0i_{13/2}$  effective single-particle energy (ESPE) in the isotonic chain together with the energy of the  $3^-$  state in the corresponding  $N = 82$  nucleus. It can be seen that, as the  $3^-$  excitation decreases in energy with  $Z$ , it reaches values comparable to ESPE for  $Z > 58$ . As a result, sizeable admixtures of the  $3^- \otimes 1f_{7/2}$  configuration into the  $13/2_1^+$  wavefunction are to be expected. Figure 7 also displays the excitation energies of the yrast  $2^+$  and  $4^+$  levels in the  $N = 82$  isotones. These energies increase with  $Z$  and reach near-constant values for  $Z > 56$ . Consequently, excitations involving the  $2^+$  and  $4^+$  core states should be expected to play a significant role where they are lowest in excitation energy. Hence, admixtures of the type  $2^+ \otimes 0i_{13/2}$  and  $4^+ \otimes 0i_{13/2}$  are to be expected in addition to the  $3^- \otimes 1f_{7/2}$  one in the wavefunctions of the  $13/2_1^+$  and  $13/2_2^+$  states with relative contributions varying with  $Z$ . Shell-model calculations reflect these observations. In the case of  $^{137}\text{Xe}$ , for example, the calculated wavefunction of the  $13/2_2^+$  level contains amplitudes of 34, 31, and 10% respectively for the  $4^+ \otimes 0i_{13/2}$ ,  $2^+ \otimes 0i_{13/2}$ , and  $3^- \otimes 1f_{7/2}$  configurations, as compared to a value of 5% for the  $0^+ \otimes 0i_{13/2}$  component. The wavefunction of the  $13/2_1^+$  state, on the other hand, is dominated by the  $i_{13/2}$  orbital, with the  $0^+ \otimes 0i_{13/2}$  component representing an amplitude of 77%, while the other significant components,  $2^+ \otimes 0i_{13/2}$  and  $4^+ \otimes 0i_{13/2}$ , contribute together a value of 15%.

Finally, the new information on negative-parity levels in  $^{137}\text{Xe}$  is discussed. Here, the focus is on the higher-lying  $3/2^-$  and  $5/2^-$  levels, but other states are considered as well. The calculated excitation energies are compared with those obtained from the experiment in Table IV. Here, the “calc2” values are reported, but there are no significant differences with “calc1” results, except for the  $13/2^+$  states discussed above. Irrespective of certain ambiguities in the experimental spin values, the observed and calculated  $3/2^-$  and  $5/2^-$  levels are reasonably close, with discrepancies of 200 keV or less. The candidate  $11/2_2^-$  level at 1879 keV can be associated with a 1759-keV state, increasing the confidence in the

proposed assignment. This state has a  $2^+ \otimes 1f_{7/2}$  “core excited” configuration as does the  $11/2_1^-$  state.

## V. CONCLUSIONS

The  $13/2_2^+$  level and a couple of new  $3/2^-$  and  $5/2^-$  levels in  $^{137}\text{Xe}$  have been observed by using a  $^{136}\text{Xe}$  beam and  $^{13}\text{C}$  and  $^9\text{Be}$  targets and performing particle- $\gamma$  coincidence measurements with the PhoswichWall and Digital Gammasphere detector arrays. The observation of the  $13/2_2^+$  level adds important information to the otherwise detailed knowledge of the  $^{137}\text{Xe}$  level scheme. The shell-model calculations performed in the course of this work focussed on systematics of the  $13/2_1^+$  and  $13/2_2^+$  levels in  $^{137}\text{Xe}$  and neighboring  $N = 83$  nuclei. Their primary outcome is to provide a realistic range for the  $\nu 0i_{13/2}$  single-particle energies ( $2360 \text{ keV} \leq E_{SPE}(\nu 0i_{13/2}) \leq 2600 \text{ keV}$ ). Specifically, the lower-limit value of this range is based on the present calculations, which are guided by the  $13/2_1^+$  level energy. The reasonable agreement of the calculations with the experimental  $13/2_2^+$  level energies, including that of the newly observed one in  $^{137}\text{Xe}$ , and additional comparisons with related levels in  $^{134,135}\text{Sb}$  support this range of values further. The calculations further support the view that couplings of core excitations with  $i_{13/2}$  and  $f_{7/2}$  neutrons contribute to the wavefunctions of these two states and that the associated amplitudes change as a function of  $Z$ .

Furthermore, it is demonstrated that the population patterns of the  $j_>$  and  $j_<$  single-particle states in  $^{137}\text{Xe}$  differ significantly depending on whether a  $^{13}\text{C}$  or a  $^9\text{Be}$  target (differing in the valence-neutron  $j$  value) is used. Hence, the “two-target” approach may well be instrumental in identifying the dominant single-particle character of a specific excitation. The technique clearly has potential for nuclear structure investigations using direct reactions with low-intensity rare-isotope beams.

### Acknowledgments

The authors thank J. T. Anderson and M. B. Oberling (ANL) for technical support and J. P. Greene (ANL) for the preparation of the targets. This work was supported by the U.S. Department of Energy, Office of Science, Office of Nuclear Physics under Grant number DE-SC0014442 and Contract numbers DE-AC02-06CH11357 and DE-AC05-00OR22725. This

research used resources of ANL's ATLAS facility, which is a DOE Office of Science User Facility.

- 
- [1] D. C. Radford *et al.*, Nucl. Phys. A **752**, 264c (2005).
  - [2] B. P. Kay *et al.*, Phys. Lett. B **658**, 216 (2008).
  - [3] B. P. Kay *et al.*, Phys. Rev. C **84**, 024325 (2011).
  - [4] J. M. Allmond *et al.*, Phys. Rev. C **86**, 031307(R) (2012).
  - [5] J. M. Allmond *et al.*, Phys. Rev. Lett. **112**, 172701 (2014).
  - [6] L. Coraggio, A. Covello, A. Gargano, and N. Itaco, Phys. Rev. C **87**, 021301(R) (2013).
  - [7] L. Coraggio, A. Covello, A. Gargano, and N. Itaco, Phys. Rev. C **87**, 034309 (2013).
  - [8] W. Urban *et al.*, Eur. Phys. J. A **5**, 239 (1999).
  - [9] B. Fornal *et al.*, Phys. Rev. C **63**, 024322 (2001).
  - [10] A. Korgul, P. Baczyk, W. Urban, T. Rzaca-Urban, A. G. Smith, and I. Ahmad, Phys. Rev. C **91**, 027303 (2015); this paper often uses  $f_{5/2}$  instead of  $f_{7/2}$ .
  - [11] K. Heyde, M. Waroquier, and H. Vincx, Phys. Lett. B **57**, 429 (1975); and references therein.
  - [12] P. J. Daly *et al.*, Phys. Rev. C **59**, 3066 (1999).
  - [13] B. Fogelberg and H. Tovedal, Nucl. Phys. A **345**, 13 (1980).
  - [14] NNDC database, <http://www.nndc.bnl.gov/nudat2>.
  - [15] G. R. Satchler, Direct Nuclear Reactions, Clarendon Press (1983); see specifically Chapter 16.
  - [16] J. T. Anderson *et al.*, 2012 IEEE Nuclear Science Symposium and Medical Imaging Conference Record (NSS/MIC), N20-2, P. 1536; and references therein.
  - [17] The most downstream ring of Digital Gammasphere was not used.
  - [18] D. G. Sarantites, W. Reviol, J. M. Elson, J. E. Kinnison, C. J. Izzo, J. Manfredi, J. Liu, H. S. Jung, and J. Goerres, Nucl. Inst. Meth. A **790**, 42 (2015).
  - [19] K. J. Honkanen, F. A. Dilmanian, D. G. Sarantites, and S. P. Sorensen, Nucl. Inst. Meth. A **257**, 233 (1987).
  - [20] D. C. Radford, Nucl. Inst. Meth. A **361**, 297 (1995).
  - [21] I. J. Thompson, Comput. Phys. Rep. **7**, 167 (1988).
  - [22] R. Machleidt, Phys. Rev. C **63**, 024001 (2001).
  - [23] F. Andreozzi, L. Coraggio, A. Covello, A. Gargano, and A. Porrino, Phys. Rev. C **56**, R16

(1997).

[24] J. Shergur *et al.*, Phys. Rev. C **71**, 064321 (2005).

TABLE I: Information for selected  $\gamma$ -ray transitions in  $^{137}\text{Xe}$  from the present work. The table is organized according to the level schemes of Fig. 3.

$E$ (keV) <sup>a</sup>	$I_i^\pi \rightarrow I_f^\pi$ <sup>b</sup>	$E_\gamma$ (keV)	$I_\gamma$ <sup>c</sup>	$A_2/A_0$	$A_4/A_0$
<i>(a) <math>^{13}\text{C}</math> Target</i>					
1220	$11/2_1^- \rightarrow 7/2^-$	1220.1(5)	71(4)	$-0.049_{-0.039}^{+0.034}$	$0.011_{-0.039}^{+0.034}$
1620	$15/2^- \rightarrow 11/2_1^-$	399.9(3)	9.7(11)	$-0.023_{-0.023}^{+0.027}$	$0.048_{-0.049}^{+0.029}$
1753	$13/2_1^+ \rightarrow 11/2_1^-$	532.7(3)	61(4)	$0.085_{-0.032}^{+0.024}$ <sup>d</sup>	-
3137 <sup>e</sup>	$13/2_2^+ \rightarrow 13/2_1^+$	1384(1) <sup>f</sup>	9.1(11)	$-0.229_{-0.045}^{+0.044}$	$0.132_{-0.069}^{+0.046}$
<i>(b) <math>^9\text{Be}</math> target</i>					
601	$3/2^- \rightarrow 7/2^-$	601.1(4)	100(4)	$\sim 0$	-
986	$1/2^- \rightarrow 3/2_1^-$	385.3(3)	71(3)	$\sim 0$	-
1220	$11/2_1^- \rightarrow 7/2^-$	1220.1(5)	9.6(10)	-	-
1753	$13/2_1^+ \rightarrow 11/2_1^-$	532.7(3)	4.3(6)	-	-
1850	$3/2^-, 5/2^- \rightarrow 1/2^-$	863(1) <sup>f</sup>	4.2(5)	-	-
1936	$5/2^- \rightarrow 1/2^-$	951(1)	10(1)	$-0.113_{-0.011}^{+0.007}$	$0.029_{-0.011}^{+0.011}$
2310 <sup>e</sup>	$- \rightarrow 1/2^-$	1324(2) <sup>f</sup>	4.3(5)	-	-
2490	$3/2^- \rightarrow 1/2^-$	1504(2)	6.2(6)	$0.042_{-0.040}^{+0.027}$	$-0.039_{-0.029}^{+0.061}$
2567	$3/2^- \rightarrow 1/2^-$	1579(3) <sup>f</sup>	4.7(5)	$0.140_{-0.098}^{+0.090}$	$0.178_{-0.089}^{+0.148}$
2949 <sup>e</sup>	$- \rightarrow 1/2^-$	1963(3) <sup>f</sup>	3.4(5)	-	-
2949 <sup>e</sup>	$- \rightarrow 3/2^-$	2349(3) <sup>f</sup>	2.1(4)	-	-

<sup>a</sup>Energy of the depopulated state.

<sup>b</sup>Spins and parities of the levels linked by the transition involved.

<sup>c</sup>Relative  $\gamma$ -ray intensity of the transition normalized to 100 for the 601-keV ground-state transition.

<sup>d</sup> $A_4$  coefficient consistent with 0.

<sup>e</sup>Newly observed level.

<sup>f</sup>Newly observed  $\gamma$  ray.

TABLE II: Measured relative yields (normalized net total intensities) and results of DWBA calculations for prominent states in the one-neutron transfer study of  $^{137}\text{Xe}$ .

$E$ (keV)	$I^\pi$	$^{13}\text{C}$ target			$^9\text{Be}$ target		
		$I_{net}^a$	$I_{net}^{rel\ b}$	$\sigma_{DWBA}^{rel\ c}$	$I_{net}^a$	$I_{net}^{rel\ b}$	$\sigma_{DWBA}^{rel\ c}$
986	$1/2^-$	47(4)	100(9)	100	32(3)	100(11)	100
1303	$5/2_1^-$	27(4)	58(8)	80	39(5)	124(14)	120
1753	$13/2_1^+$	52(4)	111(8)	89	4.3(6)	14(2)	8

<sup>a</sup>Decay intensity of the level minus the observed feeding intensity.

<sup>b</sup>Net intensity normalized to 100 for the  $1/2^-$  level.

<sup>c</sup>Relative cross section calculated for the level normalized to 100 for the  $1/2^-$  state.

TABLE III: A comparison of calculated and experimental energies of states in  $^{134}\text{Sb}$  and  $^{135}\text{Sb}$  associated with the  $i_{13/2}$  neutron orbital.

Nucleus	$I^\pi$	$E$ (keV)		
		Calc. 1	Calc. 2	Expt.
$^{134}\text{Sb}$	$10^+$	2824 <sup>a</sup>	2515	2713 <sup>b</sup>
$^{135}\text{Sb}$	$27/2^-$	3557	3468	3249 <sup>c</sup>
$^{135}\text{Sb}$	$29/2^-$	4416	4119	3688 <sup>c</sup>

<sup>a</sup>Ref. [6].

<sup>b</sup>Adopted value based on the information in Refs. [8, 9, 24].

<sup>c</sup>Ref. [10].

TABLE IV: A Comparison of calculated and experimental energies in  $^{137}\text{Xe}$ . Note that the former ones are “calc2” values (see text).

<i>calculation</i>		<i>experiment</i>	
$I^\pi$	$E$ (keV)	$I^\pi$	$E$ (keV)
$3/2_1^-$	729	$3/2_1^-$	601 <sup>a</sup>
$3/2_2^-$	1709	(3/2)	1668 <sup>a</sup>
$3/2_3^-$	1783	$3/2^-, 5/2^-$	1716 <sup>a</sup>
$3/2_4^-$	2063	( $3/2^-$ )	1842 <sup>a</sup>
$3/2_5^-$	2186	$3/2^-, 5/2^-$	1850 <sup>a</sup>
$3/2_6^-$	2233	$3/2^-$	2196 <sup>a</sup>
$3/2_7^-$	2287	$3/2^-$	2490
$3/2_8^-$	2343	3/2	2567
$5/2_1^-$	1345	$5/2_1^-$	1303 <sup>ab</sup>
$5/2_2^-$	1664	$5/2^-, 7/2^-$	1534 <sup>b</sup>
$5/2_3^-$	1795	$3/2^-, 5/2^-$	1716 <sup>a</sup>
$5/2_4^-$	1890	$3/2^-, 5/2^-$	1850 <sup>a</sup>
$5/2_5^-$	2039	$5/2^-$ <sup>c</sup>	1936 <sup>a</sup>
$7/2_2^-$	1589	$5/2^-, 7/2^-$	1534 <sup>b</sup>
$9/2_1^-$	1324	$9/2_1^-$	1218 <sup>ab</sup>
$9/2_2^-$	1584	( $9/2_2^-$ )	1590 <sup>b</sup>
$11/2_1^-$	1452	$11/2_1^-$	1220 <sup>a</sup>
$11/2_2^-$	1760	( $11/2$ ) <sup>d</sup>	1879 <sup>a</sup>
$13/2_1^+$	1786 <sup>e</sup>	$13/2_1^+$	1753 <sup>af</sup>
$13/2_2^+$	3308 <sup>e</sup>	$13/2_2^+$	3137

<sup>a</sup>Ref. [14].

<sup>b</sup>Ref. [3].

<sup>c</sup>New spin-parity assignment, cf. Table I.

<sup>d</sup>Tentative spin assignment based on intensity considerations.

<sup>e</sup>Cf. Fig. 6.

<sup>f</sup>Ref [4].

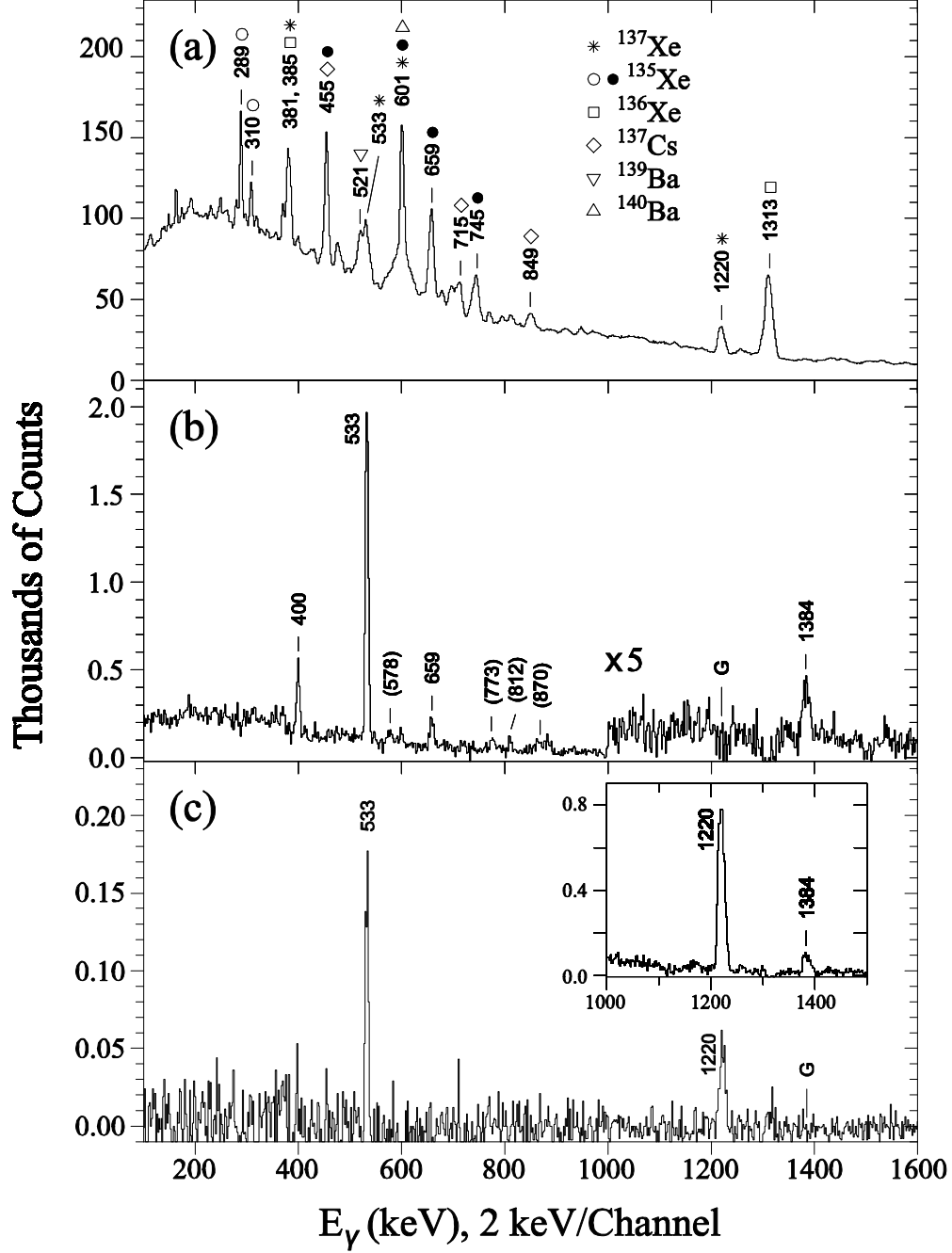


FIG. 1: Representative  $\gamma$ -ray spectra for the 560-MeV  $^{136}\text{Xe} + ^{13}\text{C}$  reaction. (a) Total projection of a  $\gamma$ - $\gamma$  coincidence matrix gated with carbon ions in the A-C map (see text). Transitions are labeled by their energies in keV. For  $^{135}\text{Xe}$ , the open and filled symbols indicate firm and tentative assignments, respectively. (b) Coincidence spectrum for  $^{137}\text{Xe}$  obtained by gating on the 1220-keV transition. Note the change in scale at a  $\gamma$ -ray energy of 1000 keV. Transitions with labels given in parentheses are associated with an interfering 1218-keV line (see text). (c) Similar to (b), but with gating transitions of 1384 (main panel) and 533 keV (inset). The position of the gate is indicated by the letter G.

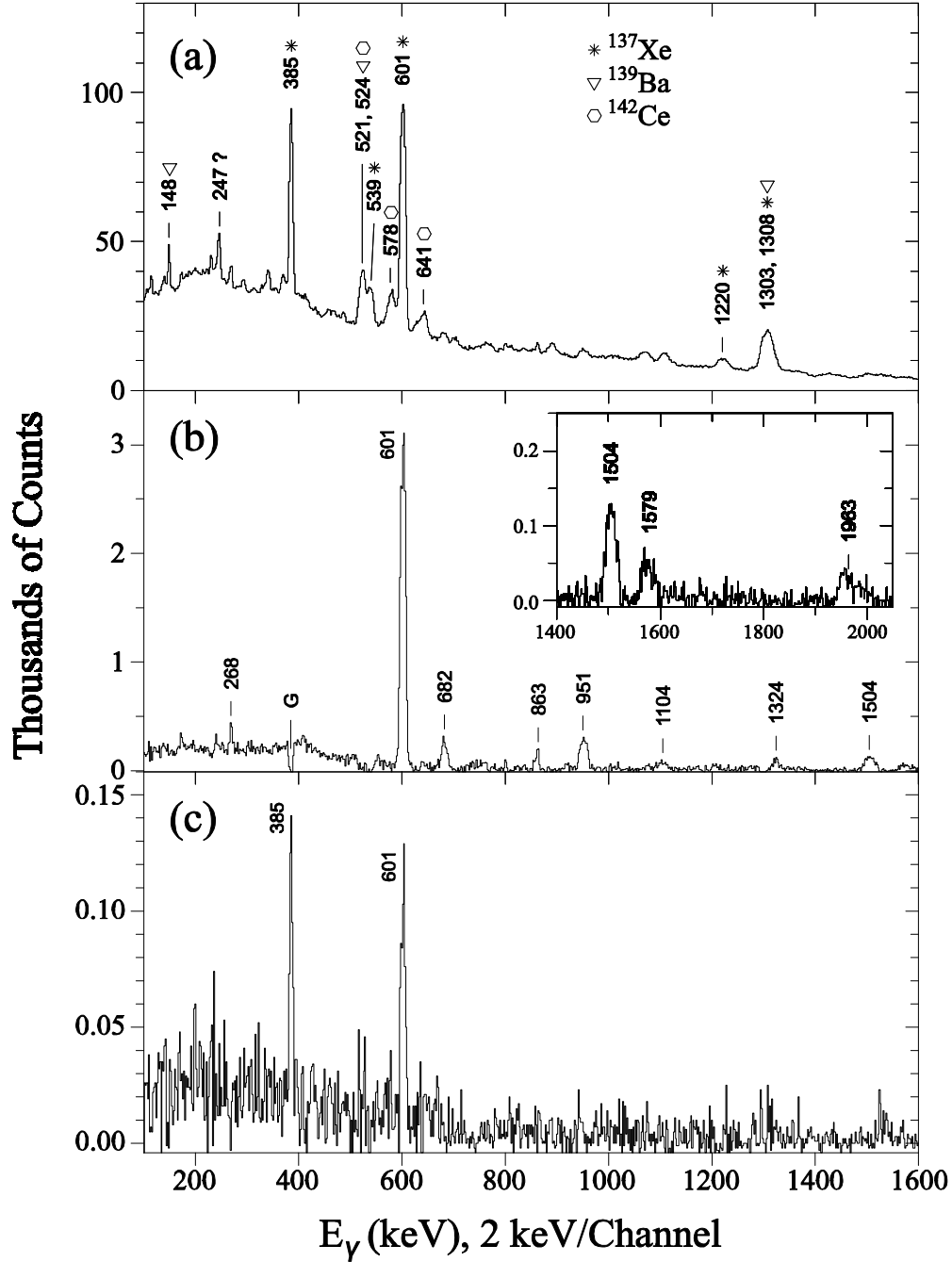
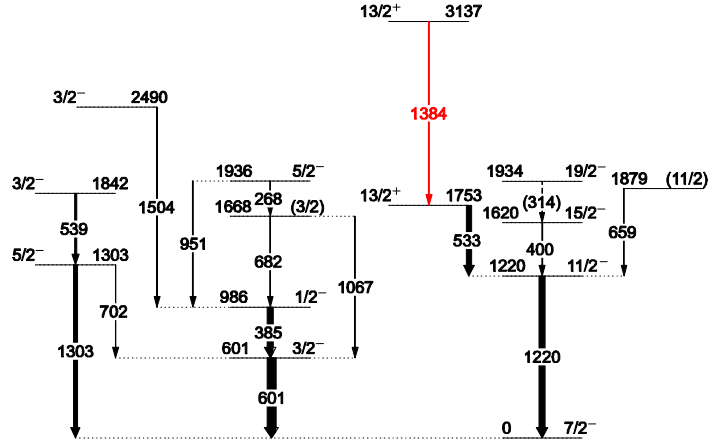


FIG. 2: Representative  $\gamma$ -ray spectra for the 560-MeV  $^{136}\text{Xe} + ^9\text{Be}$  reaction. (a) Total projection of a  $\gamma$ - $\gamma$  matrix gated on  $2a$  events (see text). Note that the 1303-keV peak is composed of a  $^{137}\text{Xe}$  ground-state transition and  $^{139}\text{Ba}$  lines with  $1306 \text{ keV} \leq E_\gamma \leq 1319 \text{ keV}$ . (b) Coincidence spectrum for  $^{137}\text{Xe}$  obtained by gating on the 385-keV transition. The inset provides the extension of the spectrum toward higher energies, the letter G indicates the position of the gate. (c) Similar to (b), but for the 1579-keV gating transition.

(a)



(b)

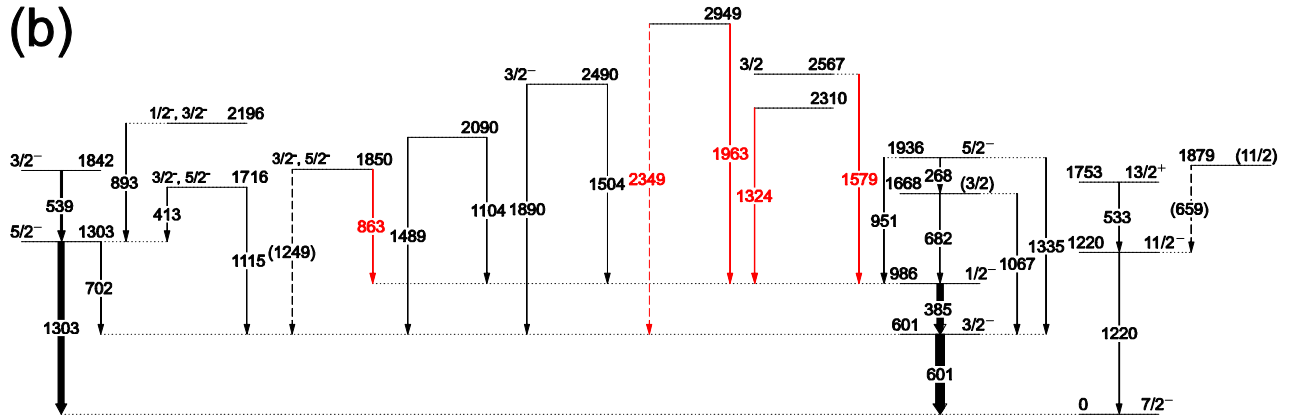


FIG. 3: The level scheme for  $^{137}\text{Xe}$  obtained in the 560-MeV  $^{136}\text{Xe} + ^{13}\text{C}$  (a) and  $^{136}\text{Xe} + ^9\text{Be}$  (b) reactions. The widths of the arrows are proportional to the measured  $\gamma$ -ray intensities. The energies are in keV. The assignments given in parentheses are tentative. The transitions marked in red are new to this work.

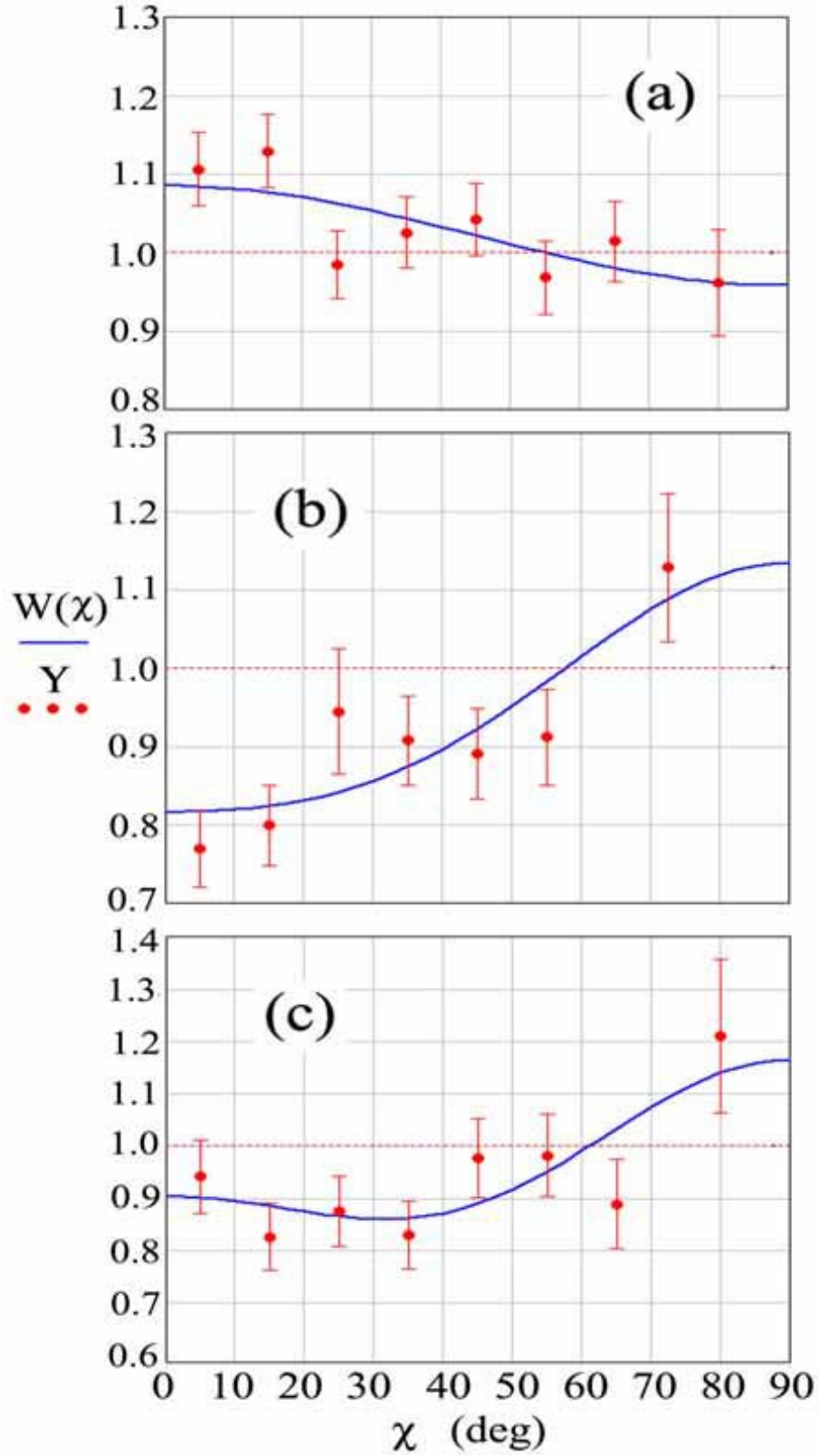


FIG. 4: Representative  $\gamma$ -ray angular distributions, with respect to the spin direction, for transitions in  $^{137}\text{Xe}$  ( $^{136}\text{Xe} + ^{13}\text{C}$  data). Panels (a) - (c) are for the 533-, 400-, and 1384-keV transitions, respectively. The former two cases are established stretched dipole ( $E1$ ) and quadrupole ( $E2$ ) transitions, respectively.

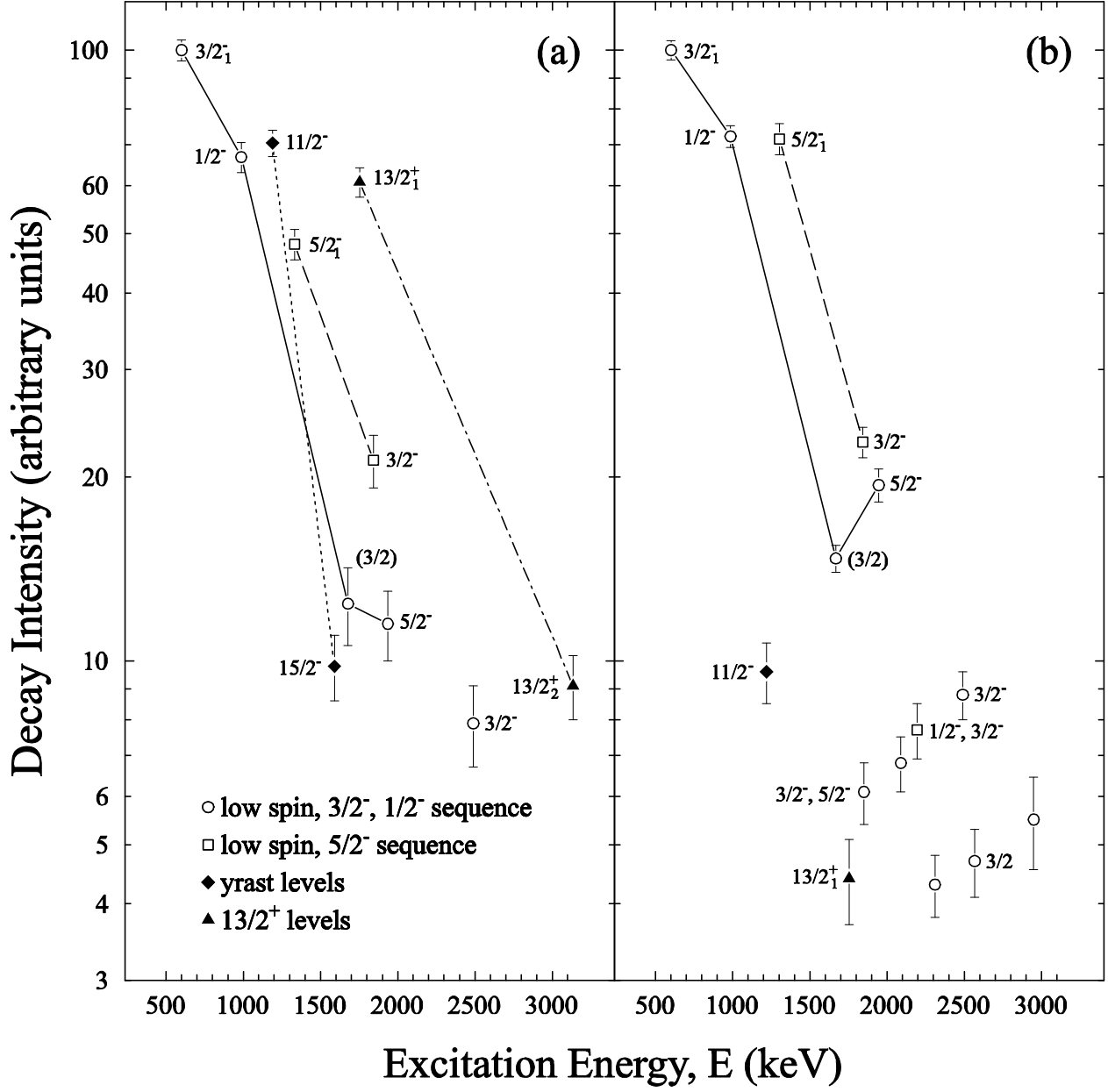


FIG. 5: Decay intensity versus energy for levels in  $^{137}\text{Xe}$  obtained in the carbon (a) and beryllium (b) measurements. The sequences of levels based on the  $3/2_1^-$  and  $1/2^-$  states, the  $5/2_1^-$  level, the  $11/2_1^-$  yrast, and the  $13/2_1^+$  unique-parity state are represented by circles, squares, diamonds, and triangles, respectively. The data points are labeled by the corresponding spin-parity assignments (except the levels in panel [b] with  $E = 2090, 2310,$  and  $2949$  keV). The most strongly populated states in a sequence are connected by straight lines.

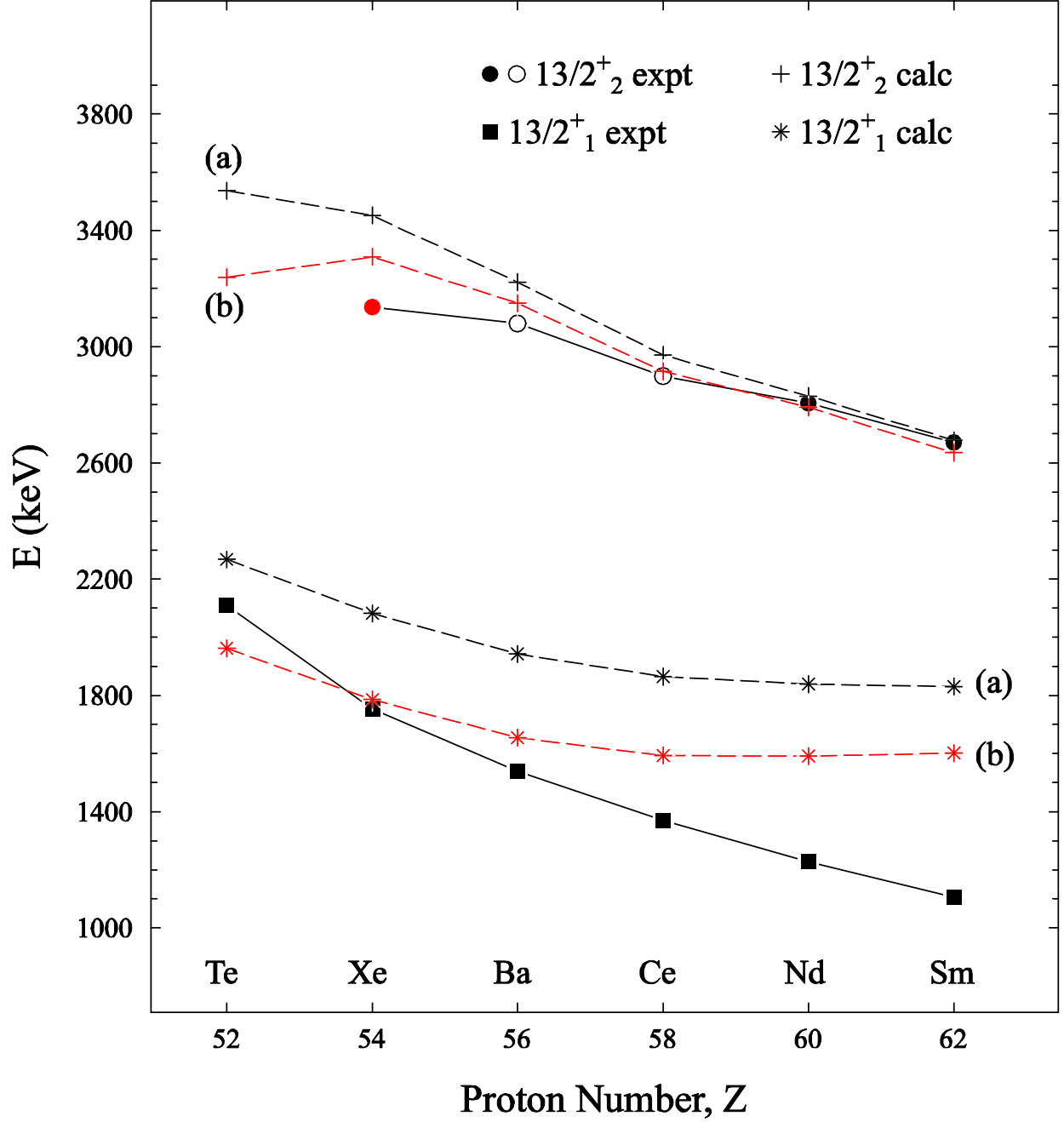


FIG. 6: The  $13/2^+_1$  and  $13/2^+_2$  systematics from Refs. [4, 14] and the present data (red circle), and results from two sets of calculations described in Ref. [6] and in the text (red crosses and asterisks), and presented in the text as “calc1” (a) and “calc2” (b), respectively. The filled and open circles distinguish between firmly established and candidate  $13/2^+_2$  levels, respectively. See text for details.

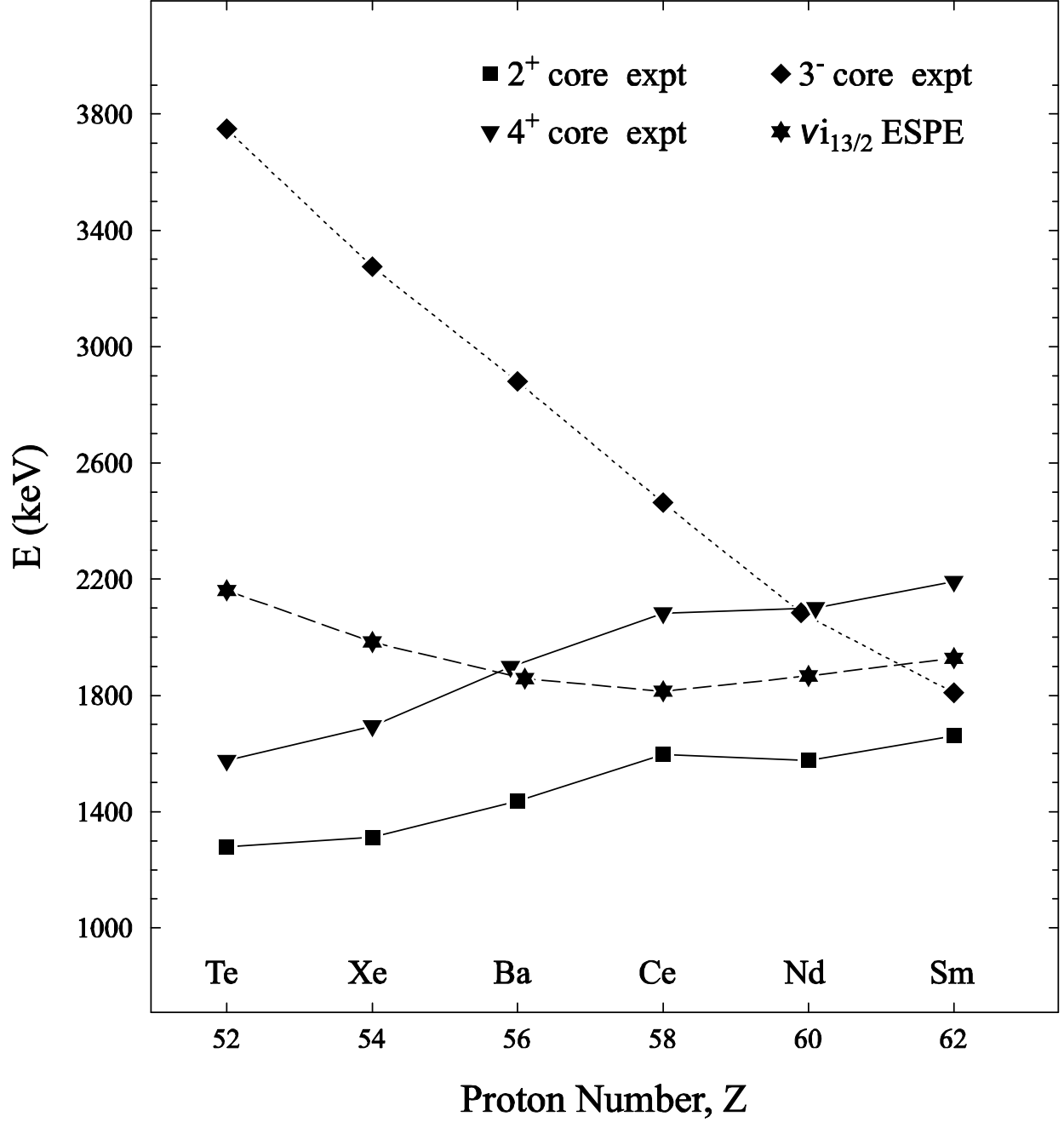


FIG. 7: A combined plot similar to Fig. 6. Shown are the  $\nu 0i_{13/2}$  effective single-particle energies, obtained from the “calc2” calculations, together with the  $3^-$ , and the yrast  $2^+$  and  $4^+$  energy levels in the corresponding  $N = 82$  core nuclei as reported in Refs. [4, 14].